

Tunable spin–spin interactions and entanglement of ions in separate potential wells

 A. C. Wilson¹, Y. Colombe¹, K. R. Brown², E. Knill¹, D. Leibfried¹ & D. J. Wineland¹

Quantum simulation^{1,2}—the use of one quantum system to simulate a less controllable one—may provide an understanding of the many quantum systems which cannot be modelled using classical computers. Considerable progress in control and manipulation has been achieved for various quantum systems^{3–5}, but one of the remaining challenges is the implementation of scalable devices. In this regard, individual ions trapped in separate tunable potential wells are promising^{6–8}. Here we implement the basic features of this approach and demonstrate deterministic tuning of the Coulomb interaction between two ions, independently controlling their local wells. The scheme is suitable for emulating a range of spin–spin interactions, but to characterize the performance of our set-up we select one that entangles the internal states of the two ions with a fidelity of 0.82(1) (the digit in parentheses shows the standard error of the mean). Extension of this building block to a two-dimensional network, which is possible using ion-trap microfabrication processes⁹, may provide a new quantum simulator architecture with broad flexibility in designing and scaling the arrangement of ions and their mutual interactions. To perform useful quantum simulations, including those of condensed-matter phenomena such as the fractional quantum Hall effect, an array of tens of ions might be sufficient^{4,10,11}.

The use of effective spin–spin interactions between ions in separate potential wells is a key feature of proposals for simulation with two-dimensional systems of quantum spins with arbitrary conformations and versatile couplings^{6,7,12}. In addition, these effective spin–spin interactions may enable logic operations to be performed in a multi-zone quantum information processor^{13–15} without the need to bring the quantum bits (qubits) into the same trapping potential well^{16,17}. Such coupling might also prove useful for metrology and sensing. For example, it could extend the capabilities of quantum-logic spectroscopy^{18,19} to ions that cannot be trapped within the same potential as the measurement ion, such as oppositely charged ions or even antimatter particles¹⁸. Coupling could be obtained either through mutually shared electrodes^{18,20} or directly through the Coulomb interaction^{13,21}.

In the experiments described here, two ions of mass m are trapped at equilibrium distance d_0 in independent, approximately harmonic potential wells. Coulomb interaction between the ions leads to dipole–dipole-type coupling, with strength $\Omega_{\text{ex}} \propto d_0^{-3}$ (Methods), where the oscillations of the ions in their respective wells manifest the dipoles¹². The coupled system has six normal modes, four perpendicular to the direction between the double wells (radial) and two along this direction (axial). Although all these modes are useful for dipole–dipole coupling¹², we concentrate on the two axial modes, with uncoupled well frequencies $\omega_l \approx \omega_r$, and with eigenfrequencies and eigenvectors

$$\begin{aligned} \omega_{\text{str}} &= \bar{\omega} + \sqrt{\delta^2 + \Omega_{\text{ex}}^2} \\ \omega_{\text{com}} &= \bar{\omega} - \sqrt{\delta^2 + \Omega_{\text{ex}}^2} \\ q_{\text{str}} &= (\sin(\theta_{\text{str}}), \cos(\theta_{\text{str}})) \\ q_{\text{com}} &= (\sin(\theta_{\text{com}}), \cos(\theta_{\text{com}})) \end{aligned} \quad (1)$$

where $\theta_{\text{str}} = \arctan \left[\left(\delta - \sqrt{\delta^2 + \Omega_{\text{ex}}^2} \right) / \Omega_{\text{ex}} \right]$ and $\theta_{\text{com}} = \arctan \left[\left(\delta + \sqrt{\delta^2 + \Omega_{\text{ex}}^2} \right) / \Omega_{\text{ex}} \right]$. The average well frequency is denoted by $\bar{\omega} \equiv (\omega_l + \omega_r)/2$, and the frequency difference is $2\delta = (\omega_r - \omega_l)$. For $|\delta| \gg \Omega_{\text{ex}}$ these modes decouple and the two ions move nearly independently of each other. When approaching resonance ($\delta = 0$), the motions of the ions are strongly coupled, resulting in an avoided crossing of the motional frequencies with a splitting of $2\Omega_{\text{ex}}$. On resonance, the normal modes are a centre-of-mass mode ($\omega_{\text{com}}, q_{\text{com}} = (1/\sqrt{2}, 1/\sqrt{2})$) and a stretch mode ($\omega_{\text{str}}, q_{\text{str}} = (-1/\sqrt{2}, 1/\sqrt{2})$), with motional quanta shared between the two ions.

These shared quantized degrees of freedom can simulate spin–spin interactions^{5,22,23}, just as for two-qubit quantum logic gates with ions in the same harmonic well; but, unlike in the latter case, the strength of the spin–spin interaction can be tuned from strong to weak by controlling the individual trapping wells^{12,16,17}. We denote the energy eigenstates of the pseudo-spin-1/2 systems as $\{|\uparrow\rangle, |\downarrow\rangle\}$, corresponding to internal states of the ions, separated by $\hbar\omega_0$ (\hbar , Planck’s constant divided by 2π), and the number states of the normal modes as $|n_{\text{str}}\rangle$ and $|n_{\text{com}}\rangle$. We excite ‘carrier’ transitions $|\downarrow, n_{\text{str}}, n_{\text{com}}\rangle \leftrightarrow |\uparrow, n_{\text{str}}, n_{\text{com}}\rangle$ with a uniform oscillating field at the $|\downarrow\rangle \leftrightarrow |\uparrow\rangle$ transition frequency ω_0 , and with phase ϕ_c . Simultaneously, a single ‘red-sideband’ excitation at frequency $\omega_0 - \bar{\omega}$ and phase ϕ_s , between the sideband frequencies for the stretch and centre-of-mass modes, excites both the $|\downarrow, n_{\text{str}}, n_{\text{com}}\rangle \leftrightarrow |\uparrow, n_{\text{str}} - 1, n_{\text{com}}\rangle$ transition and the $|\downarrow, n_{\text{str}}, n_{\text{com}}\rangle \leftrightarrow |\uparrow, n_{\text{str}}, n_{\text{com}} - 1\rangle$ transition^{24,25}. These excitations emulate an effective spin–spin interaction (Methods)

$$\begin{aligned} \hat{H}_{\text{eff}} &= \hbar\kappa \hat{\sigma}_1^{\phi_c} \hat{\sigma}_r^{\phi_c} \\ \hat{\sigma}_{1/r}^{\phi_c} &= \cos(\phi_c) \hat{\sigma}_{1/r}^x - \sin(\phi_c) \hat{\sigma}_{1/r}^y \end{aligned}$$

where κ is the coupling strength and $\hat{\sigma}_{1/r}^{x/y}$ are the Pauli spin-1/2 operators of the respective ions. We can emulate antiferromagnetic ($\kappa > 0$) and ferromagnetic ($\kappa < 0$) interactions by our choice of the ion spacing or the detunings δ_{str} and δ_{com} of the normal modes relative to the sideband drive (Methods). Under the simultaneous carrier and red-sideband drive, the spins become periodically entangled and disentangled with the motion. Starting with a product state $|\Phi_i\rangle$, spins and motion are disentangled into a product state at $T_j = 2\pi j/\Omega_{\text{ex}}$ ($j > 0$ integer), but the spins acquire phases that depend on the ions’ motion in phase space during the off-resonance excitation. These phases simulate the spin–spin interaction²⁶. We benchmark our implementation of the spin–spin interaction by starting from the well-defined product state $|\Psi_i\rangle = |\downarrow\downarrow\rangle$, effectively evolving it under an antiferromagnetic ($\kappa > 0$) interaction for time $T_2 = \pi/4\kappa$ with $\phi_c = 0$, and comparing the resulting state with the maximally entangled state $|\Psi_e\rangle = \exp \left[-i \frac{\pi}{4} \hat{\sigma}_1^x \hat{\sigma}_r^x \right] |\Psi_i\rangle = \frac{1}{\sqrt{2}} (|\downarrow\downarrow\rangle - i|\uparrow\uparrow\rangle)$ that would be produced under ideal conditions (Methods).

The (pseudo-)spin-1/2 system is formed by the $|2s^2S_{1/2}, F = 1, m_F = -1\rangle \equiv |\uparrow\rangle$ and $|2s^2S_{1/2}, F = 2, m_F = -2\rangle \equiv |\downarrow\rangle$ hyperfine ground

¹National Institute of Standards and Technology, 325 Broadway, Boulder, Colorado 80305, USA. ²Georgia Tech Research Institute, 400 10th Street Northwest, Atlanta, Georgia 30332, USA.

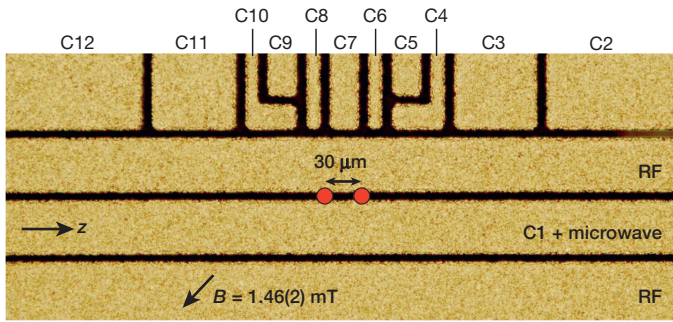


Figure 1 | Microfabricated surface-electrode trap. Microscope image of ion-trap electrodes, showing radio-frequency (RF) and static-potential control electrodes (C1–C12). Dark areas are the 5 μm gaps between electrodes. Ions are trapped 40 μm above the chip surface; red dots indicate the ion locations, with a 30 μm spacing. Electrode C1 also supports microwave currents at 1.28 GHz to drive carrier transitions on the two ions.

states of ${}^9\text{Be}^+$, where F is the total angular momentum and m_F is the component of F along a quantization axis provided by a 1.46(2) mT static magnetic field (Fig. 1). The ions are confined in a cryogenic (trap temperature < 5 K), microfabricated, surface-electrode linear Paul ion trap¹⁶ composed of 10 μm -thick gold electrodes separated by 5 μm gaps, deposited onto a crystalline quartz substrate. An oscillating potential (~ 100 V peak at 163 MHz), applied to the radiofrequency electrodes in Fig. 1, provides pseudopotential confinement of the ions in the radial (perpendicular to z) directions at motional frequencies of ~ 17 and ~ 27 MHz at a distance of approximately 40 μm from the trap surface. Along the trap z axis, a double well is formed by static potentials applied to control electrodes C1–C12. The axial (z) oscillation frequencies ω_1 and ω_r around the respective minima are typically near 4 MHz. Single-ion heating¹³ is in the range of 100 to 200 quanta per second. This heating is approximately four orders of magnitude larger than that due to our estimate of Johnson noise heating for this apparatus. For two ions spaced 30 μm apart, and in motional resonance ($\delta = 0$), the period required for the ions to exchange their motional energies is $\tau_{\text{ex}} \equiv \pi/2\Omega_{\text{ex}} = 70$ μs , compared with an average period of 5–10 ms required to absorb a single motional quantum due to background heating. Fine adjustment of control-electrode potentials (at the 100 μV level) enables individual control of potential-well curvatures to tune the Coulomb interaction between the ions through resonance. Electrode C1 also supports microwave currents (typically of milliampere amplitude) that produce an oscillating magnetic field to drive carrier transitions at the same rate in both ions.

Superimposed σ^- -polarized laser beams, nearly resonant with the $2s^2S_{1/2} \rightarrow 2p^2P_{1/2}$ and the $2s^2S_{1/2} \rightarrow 2p^2P_{3/2}$ transitions ($\lambda \approx 313$ nm) and propagating along the magnetic field direction, are used for optical pumping, Doppler laser cooling and state detection by resonance fluorescence. Optical pumping prepares both ions in $|\downarrow\rangle$. We can distinguish the $|\downarrow\rangle$ (bright) and $|\uparrow\rangle$ (dark) states by detecting resonance fluorescence on the $|\downarrow\rangle \rightarrow |2p^2P_{3/2}, F=3, m_F=-3\rangle$ optical cycling transition. Typically, three to five photons are detected per ion in $|\downarrow\rangle$ over a background of 0.15 to 0.6 photons on a photomultiplier during detection periods in the range 300–400 μs . A pair of elliptically shaped laser beams, separated in frequency by approximately the $|\downarrow\rangle \leftrightarrow |\uparrow\rangle$ transition frequency ($\omega_0 \approx 2\pi \times 1.28$ GHz) and detuned 80 GHz above the ${}^2S_{1/2} \rightarrow {}^2P_{1/2}$ transition, illuminate both ions with equal intensity. These beams induce two-photon stimulated-Raman transitions for ground-state cooling¹³ and for the motional sideband excitations used to implement the spin-spin interaction²⁶. Derived from the same 313 nm source, the frequency difference between the beams is produced with acousto-optic modulators, and the beam orientation is such that the difference wavevector $k = k_2 - k_1$ is parallel to the z axis (with magnitude $k = 2\sqrt{2}\pi/\lambda$). The spin-spin coupling strength is $\kappa = \cos(2\phi)(\eta\Omega_s)^2/2\Omega_{\text{ex}}$, where $2\phi = kd_0$ is the phase difference of the beat note between the two laser fields at the positions of the ions, Ω_s is the stimulated-Raman Rabi frequency and $\eta = k/\sqrt{\hbar/2m\bar{\omega}}$ (Methods).

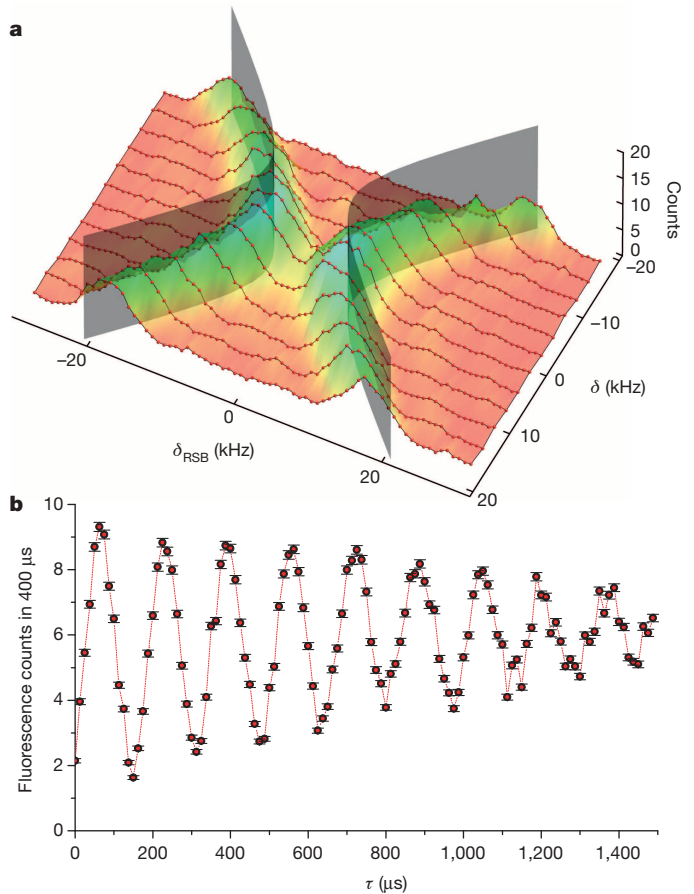


Figure 2 | Motional spectroscopy of two coupled ions. **a**, The red dots connected by black lines indicate separate scans of the red-sideband detuning δ_{RSB} from the average mode frequency $\bar{\omega}$ for different values of the difference δ between the individual well frequencies. The vertical scale is proportional to the sum of the probabilities for each ion to be in $|\downarrow\rangle$. At the centre of the avoided crossing, the normal mode frequency splitting Ω_{ex}/π is 12(1) kHz. Each data point represents an average of 200 experiments. Shaded planes are a theoretical prediction for the avoided crossing according to equations (1). **b**, Resonant ($\delta \approx 0$) single-quantum motional exchange between two ions, with an exchange time $\tau_{\text{ex}} = 80(2)$ μs . The vertical scale is proportional to the probability of the laser-addressed ion being in $|\downarrow\rangle$. Each data point represents an average of 500 experiments, and error bars correspond to s.e.m. Dashed lines are included to guide the eye.

A key to implementing spin–spin interactions with ions in separate trapping zones is being able to tune the well frequencies precisely enough to control the eigenfrequencies and eigenmodes (equations (1)) near the avoided crossing. In Fig. 2a, we characterize this avoided crossing. For these experiments, the ions are separated by 27(2) μm . They are laser-cooled nearly to their motional ground states (mean motional mode occupation, $\bar{n}_{\text{str/com}} \approx 0.1$), optically pumped to the $|\downarrow\downarrow\rangle$ state and then rotated into the $|\uparrow\uparrow\rangle$ state with a microwave carrier π -pulse. Fine adjustments are made to control electrodes C2 and C12 to tune the harmonic confinement of the two trapping zones, stepping the system through the avoided crossing. At each step, after cooling and optical pumping, we implement the Raman red-sideband drive and scan its detuning δ_{RSB} with respect to $\bar{\omega}$. If the sideband excitation frequency is equal to $\omega_0 - \omega_{\text{str}}$ or $\omega_0 - \omega_{\text{com}}$, then the spin of one or both ions can flip to $|\downarrow\rangle$ while absorbing quanta of motion, and a peak in the resonance fluorescence counts is observed. The spectral resolution is set by the duration of the square-pulse sideband excitation (120 μs). At the centre of the avoided crossing, the splitting of the mode frequencies is $2\Omega_{\text{ex}} = 2\pi \times 12(1)$ kHz.

In Fig. 2b, we show data that demonstrate single-phonon exchange between the two ions. With the trapping zones tuned to resonance ($\delta = 0$), both modes are cooled to near the motional ground state and the ions

are prepared in $|\uparrow\uparrow\rangle$. In this experiment, the two Raman beams are tightly focused onto only one of the ions and are used to add a single phonon to that ion (and flip its spin) with a π -pulse on the red sideband of its local frequency in a duration short compared with τ_{ex} . In this limit, after the pulse, the resulting motional state is an equal superposition of both modes, and the phonon energy is therefore exchanged between the ions with a period $2\tau_{\text{ex}}$ (ref. 16). To monitor the exchange, the same Raman interaction is applied again after a variable delay τ . This can flip the spin and remove the quantum of motion only if the motion resides solely in the addressed ion after a particular delay. The level of fluorescence is proportional to the probability of this spin flip. From this, we determine an exchange time of $\tau_{\text{ex}} = 80(2) \mu\text{s}$, consistent with an ion spacing of $30(2) \mu\text{m}$ for this experiment. The reduction in contrast for longer delays is caused mainly by fluctuations and drifts of the trapping potential. We estimate that $\delta/2\pi$ drifted by approximately 500 Hz (a significant fraction of $\Omega_{\text{ex}}/2\pi$) during the 2–3 minutes required for the 20,000 experiments that provided the data for Fig. 2b.

For benchmarking the spin–spin interaction, the laser beams for fluorescence detection, Doppler cooling and stimulated Raman transitions are made to spatially overlap both ions with equal intensity. The ion spacing (approximately $27 \mu\text{m}$ here) is adjusted to an integer number of half-wavelengths of the difference wavevector of the two Raman laser fields, by a technique described elsewhere²⁷, such that $\cos(2\phi) \approx 1$. The wells are tuned to resonance ($\delta = 0$) with adjustments to control electrodes C2 and C12. The ions are first Doppler-cooled, then Raman sideband-cooled to near the ground state on both normal modes, and finally optically pumped into the $|\downarrow\downarrow\rangle$ state. The spin–spin interaction is implemented by simultaneously applying a relatively strong resonant microwave carrier excitation (Rabi frequency, $\Omega_c = 2\pi \times 23.1(2) \text{ kHz}$) and an optical sideband excitation at $\omega_0 - \bar{\omega}$ (Rabi frequency, $\eta\Omega_s = 2\pi \times 2.4(2) \text{ kHz}$). The exchange frequency satisfies $2\Omega_{\text{ex}} = 2\pi \times 13(1) \text{ kHz}$, so that $\kappa = 2\pi \times 446(13) \text{ Hz}$. In the middle of the coupling period, we shift the phases ϕ_c and ϕ_s of both driving fields by 180° relative to their phases during the first half of the coupling period. These phase reversals suppress the dependence of the final state on the carrier Rabi frequency and reduce sensitivity of the spin–spin interaction to drifts in the detuning and the coupling time (Methods). At the end of the coupling period, fluorescence detection and subsequent fitting of the photon-count histograms to those for the three possible outcomes (two ions bright, $|\downarrow\downarrow\rangle$; one ion bright, $|\downarrow\uparrow\rangle$ or $|\uparrow\downarrow\rangle$; or both ions dark, $|\uparrow\uparrow\rangle$) yield the respective probabilities P_2 , P_1 and P_0 .

Evolution of these probabilities as functions of the coupling duration is shown in Fig. 3a. Near $300 \mu\text{s}$, P_2 and P_0 are approximately equal ($P_2 + P_0 = 0.91(2)$) and P_1 has reached a minimum. To show that the resulting state is entangled, in a subsequent experiment we stop the evolution at $300 \mu\text{s}$, apply a carrier $\pi/2$ -pulse of variable phase ϕ_a , and determine the parity $\Pi = P_2 + P_0 - P_1$ as a function of ϕ_a . These data are shown in Fig. 3b together with a fit to $A\cos(2\phi_a + \phi_0) + B$. The fitted probabilities and the contrast $A = 0.73(2)$ imply a state fidelity²⁸ $F = \langle \Psi_e | \rho_e | \Psi_e \rangle = (P_2 + P_0 + A)/2 = 0.82(1)$, where the density matrix ρ_e describes the experimentally produced state (Methods). From simulations and independent measurements, we estimate the leading contributions to the observed infidelity as follows: drift and fluctuations of the trapping potentials (including ‘anomalous’ motional heating) contribute ~ 0.08 ; spontaneous emission due to off-resonance excitation by Raman laser beams contributes ~ 0.02 ; Raman laser beam intensity fluctuations contribute ~ 0.03 ; and state preparation and detection errors contribute ~ 0.03 .

For scalable implementations of lattices of interacting spins, the quality and ease of tuning of the spin–spin interaction must be improved; however, there are no apparent fundamental barriers to this. Trap potential fluctuations in our experiments appear to be dominated by changes in surface charging and work functions rather than changes in externally applied control potentials. It should be possible to suppress these fluctuations by improving the surface quality of the electrodes²⁹, reducing the amount of nearby dielectric materials and minimizing the exposure

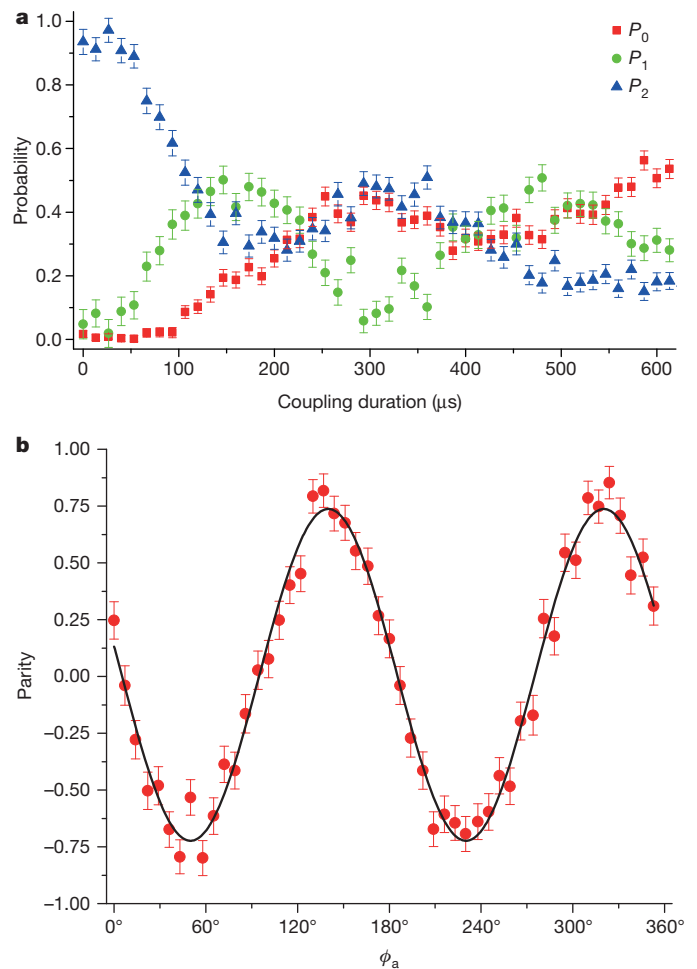


Figure 3 | Characterizing the spin–spin coupling interaction between ions in separate trapping zones. **a**, Evolution of probabilities P_0 of $|\uparrow\uparrow\rangle$ (red), P_1 of $|\downarrow\downarrow\rangle$ and $|\uparrow\downarrow\rangle$ (green), and P_2 of $|\downarrow\downarrow\rangle$ (blue), as functions of coupling duration. Each data point represents an average of 400 experiments, and error bars correspond to the s.e.m. **b**, Parity oscillation obtained (for a coupling duration of $300 \mu\text{s}$) by applying a carrier analysis $\pi/2$ -pulse with variable phase ϕ_a , and a fit to the data (black curve). Each data point represents an average of 400 experiments, and error bars correspond to the s.e.m.

of the electrodes to ultraviolet light through better beam shaping. Laser intensity and pointing noise can be reduced by passive or active stabilization of the beams with respect to the ions (or both), or potentially avoided entirely by using microwave gradient fields for the sideband interactions¹². The microfabrication techniques used to construct the trap are scalable to larger arrays of trapped ions, thus potentially enabling informative ‘analogue’ quantum simulations⁴ without requiring arbitrarily precise quantum control. Theoretical work to quantify the common belief that many observables of interest in analogue quantum simulations are sufficiently robust is ongoing³⁰ (Methods). Initial indications are that the proposed technical improvements may be sufficient. A three-by-three lattice is sufficient to simulate quantum Hall physics, and with six-by-six lattices fractional Hall effects and other intriguing solid-state phenomena become accessible^{8,11}. Even for these modest numbers of spins, modelling of quantum interactions with conventional computers is challenging; this difficulty may be overcome with quantum simulations.

Online Content Methods, along with any additional Extended Data display items and Source Data, are available in the online version of the paper; references unique to these sections appear only in the online paper

Received 5 February; accepted 2 June 2014.

1. Feynman, R. P. Simulating physics with computers. *Int. J. Theor. Phys.* **21**, 467–488 (1982).

2. Lloyd, S. Universal quantum simulators. *Science* **273**, 1073–1078 (1996).
3. Ladd, T. D. *et al.* Quantum computers. *Nature* **464**, 45–53 (2010).
4. Georgescu, I. M., Ashhab, S. & Nori, F. Quantum simulation. *Rev. Mod. Phys.* **86**, 153–185 (2014).
5. Blatt, R. & Roos, C. F. Quantum simulations with trapped ions. *Nature Phys.* **8**, 277–284 (2012).
6. Chiaverini, J. & Lybarger, W. E. Laserless trapped-ion quantum simulations without spontaneous scattering using microtrap arrays. *Phys. Rev. A* **77**, 022324 (2008).
7. Schmied, R., Wesenberg, J. H. & Leibfried, D. Optimal surface-electrode trap lattices for quantum simulation with trapped ions. *Phys. Rev. Lett.* **102**, 233002 (2009).
8. Shi, T. & Cirac, J. I. Topological phenomena in trapped-ion systems. *Phys. Rev. A* **87**, 013606 (2013).
9. Seidelin, S. *et al.* Microfabricated surface-electrode ion trap for scalable quantum information processing. *Phys. Rev. Lett.* **96**, 253003 (2006).
10. Friedenauer, A., Schmitz, H., Glueckert, J. T., Porras, D. & Schaetz, T. Simulating a quantum magnet with trapped ions. *Nature Phys.* **4**, 757–761 (2008).
11. Nielsen, A. E. B., Sierra, G. & Cirac, J. I. Local models of fractional quantum Hall states in lattices and physical implementation. *Nature Commun.* **4**, 2864 (2013).
12. Schmied, R., Wesenberg, J. H. & Leibfried, D. Quantum simulation of the hexagonal Kitaev model with trapped ions. *New J. Phys.* **13**, 115011 (2011).
13. Wineland, D. J. *et al.* Experimental issues in coherent quantum-state manipulation of trapped atomic ions. *J. Res. Natl Inst. Stand. Technol.* **103**, 259–328 (1998).
14. Cirac, J. I. & Zoller, P. A scalable quantum computer with ions in an array of microtraps. *Nature* **404**, 579–581 (2000).
15. Kielpinski, D., Monroe, C. & Wineland, D. J. Architecture for a large-scale ion-trap quantum computer. *Nature* **417**, 709–711 (2002).
16. Brown, K. R. *et al.* Coupled quantized mechanical oscillators. *Nature* **471**, 196–199 (2011).
17. Harlander, M., Lechner, R., Brownnutt, M., Blatt, R. & Hänsel, W. Trapped-ion antennae for the transmission of quantum information. *Nature* **471**, 200–203 (2011).
18. Heinzen, D. J. & Wineland, D. J. Quantum-limited cooling and detection of radio-frequency oscillations by laser-cooled ions. *Phys. Rev. A* **42**, 2977–2994 (1990).
19. Schmidt, P. O. *et al.* Spectroscopy using quantum logic. *Science* **309**, 749–752 (2005).
20. Daniilidis, N., Lee, T., Clark, R., Narayanan, S. & Häffner, H. Wiring up trapped ions to study aspects of quantum information. *J. Phys. B* **42**, 154012 (2009).
21. Ciaramicoli, G., Marzoli, I. & Tombesi, P. Scalable quantum processor with trapped electrons. *Phys. Rev. Lett.* **91**, 017901 (2003).
22. Kim, K. *et al.* Quantum simulation of frustrated Ising spins with trapped ions. *Nature* **465**, 590–593 (2010).
23. Britton, J. W. *et al.* Engineered two-dimensional Ising interactions in a trapped-ion quantum simulator with hundreds of spins. *Nature* **484**, 489–492 (2012).
24. Bermudez, A., Schmidt, P. O., Plenio, M. B. & Retzker, A. Robust trapped-ion quantum logic gates by continuous dynamical decoupling. *Phys. Rev. A* **85**, 040302(R) (2012).
25. Tan, T. R. *et al.* Demonstration of a dressed-state phase gate for trapped ions. *Phys. Rev. Lett.* **110**, 263002 (2013).
26. Porras, D. & Cirac, J. I. Effective quantum spin systems with trapped ions. *Phys. Rev. Lett.* **92**, 207901 (2004).
27. Chou, C. W., Hume, D. B., Thorpe, M. J., Wineland, D. J. & Rosenband, T. Quantum coherence between two atoms beyond $Q = 10^{15}$. *Phys. Rev. Lett.* **106**, 160801 (2011).
28. Sackett, C. A. *et al.* Experimental entanglement of four particles. *Nature* **404**, 256–259 (2000).
29. Hite, D. A. *et al.* 100-fold reduction of electric-field noise in an ion trap cleaned with in situ argon-ion-beam bombardment. *Phys. Rev. Lett.* **109**, 103001 (2012).
30. Hauke, P. *et al.* Can one trust quantum simulators? *Rep. Prog. Phys.* **75**, 082401 (2012).

Acknowledgements We thank K. McCormick, A. Keith and D. Allcock for comments on the manuscript. This research was funded by the Office of the Director of National Intelligence (ODNI), Intelligence Advanced Research Projects Activity (IARPA), ONR, and the NIST Quantum Information Program. All statements of fact, opinion or conclusions contained herein are those of the authors and should not be construed as representing the official views or policies of IARPA or the ODNI. This work, a submission of NIST, is not subject to US copyright.

Author Contributions A.C.W. and D.L. designed the experiment, developed components of the experimental apparatus, collected data, analysed results and wrote the manuscript. D.L. developed the theory. Y.C. fabricated the ion-trap chip. K.R.B. built components of the apparatus, most notably the cryostat, and participated in the early design phase of the experiment. E.K. assisted with data analysis. D.J.W. participated in the design and analysis of the experiment. All authors discussed the results and the text of the manuscript.

Author Information Reprints and permissions information is available at www.nature.com/reprints. The authors declare no competing financial interests. Readers are welcome to comment on the online version of the paper. Correspondence and requests for materials should be addressed to A.C.W. (andrew.wilson@nist.gov).

METHODS

Normal modes of the coupled wells. We consider two ions, cooled close to their motional ground states. Along the direction of separation, each ion is confined to a separate minimum of a double-well potential with minima denoted 'l' (left) and 'r' (right). We assume much stronger confinement in the remaining directions, such that it is sufficient to consider only motion along the direction of the separated double well. The Hamiltonian of the motion of two ions of mass m and charge Q , spaced at an average distance d_0 in wells with local harmonic oscillator ladder operators \hat{a}_l and \hat{a}_r and uncoupled oscillation frequencies ω_l and ω_r , including Coulomb coupling and neglecting constant energy terms, can be written for small motional excitation as¹⁶

$$\hat{H}_m = \hbar\omega_l \hat{a}_l^\dagger \hat{a}_l + \hbar\omega_r \hat{a}_r^\dagger \hat{a}_r - \hbar\Omega_{\text{ex}} \left(\hat{a}_l^\dagger \hat{a}_r + \hat{a}_r^\dagger \hat{a}_l \right)$$

with

$$\Omega_{\text{ex}} = \frac{Q^2}{4\pi\epsilon_0 m \sqrt{\omega_l \omega_r} d_0^3}$$

We define $\bar{\omega} \equiv (\omega_l + \omega_r)/2$ and $\delta = (\omega_r - \omega_l)/2$ and transform the motion into a normal-mode basis with eigenfrequencies and eigenvectors (expressed in the eigenmode basis of two uncoupled ions)

$$\omega_{\text{str/com}} = \bar{\omega} \pm \sqrt{\delta^2 + \Omega_{\text{ex}}^2}$$

$$q_{\text{str/com}} = \left(q_{\text{str/com}}^{(l)}, q_{\text{str/com}}^{(r)} \right) = \left(\sin(\theta_{\text{str/com}}), \cos(\theta_{\text{str/com}}) \right)$$

where

$$\theta_{\text{str/com}} = \arctan \left[\frac{\delta \mp \sqrt{\delta^2 + \Omega_{\text{ex}}^2}}{\Omega_{\text{ex}}} \right]$$

and the upper and lower signs apply to the stretch and centre-of-mass modes, respectively. In this basis, the motional Hamiltonian is

$$\hat{H}_m = \hbar\omega_{\text{str}} \hat{a}_{\text{str}}^\dagger \hat{a}_{\text{str}} + \hbar\omega_{\text{com}} \hat{a}_{\text{com}}^\dagger \hat{a}_{\text{com}}$$

where $\hat{a}_{\text{str/com}}$ are the corresponding ladder operators in the coupled basis. For $\delta = 0$, we recover the familiar centre-of-mass and stretch modes with a mode splitting of $2\Omega_{\text{ex}}$ and in the limit $\delta \ll \Omega_{\text{ex}}$ we can approximate

$$q_{\text{str/com}} \approx \left(\frac{\mp 1}{\sqrt{2}} \left(1 \mp \frac{\delta}{2\Omega_{\text{ex}}} \right), \frac{1}{\sqrt{2}} \left(1 \pm \frac{\delta}{2\Omega_{\text{ex}}} \right) \right)$$

Interaction Hamiltonian. The two ions are driven resonantly by a spatially uniform excitation on the carrier transition $|\uparrow_{l/r}\rangle \leftrightarrow |\downarrow_{l/r}\rangle = \hat{\sigma}_{l/r}^\dagger |\uparrow_{l/r}\rangle$ at frequency ω_0 , Rabi-frequency Ω_c and phase ϕ_c . In the interaction picture and rotating-wave approximation, the carrier interaction takes the form

$$\hat{H}_c = \hbar\Omega_c \left[(\hat{\sigma}_l^- + \hat{\sigma}_r^-) e^{-i\phi_c} + (\hat{\sigma}_l^+ + \hat{\sigma}_r^+) e^{i\phi_c} \right]$$

with $\hat{\sigma}_{l/r}^\pm = (\hat{\sigma}_{l/r}^\pm)^\dagger$. Simultaneously, the ions are driven close to the Raman red sidebands of both normal modes by two laser beams (quantities associated with which will be denoted using indices 1 and 2) with difference wavevector ($k = k_2 - k_1$; magnitude $k = 2\sqrt{2}\pi/\lambda$) aligned along the direction of the double well, having frequency difference $\Delta\omega_L = \omega_2 - \omega_1 \approx \omega_0 - \bar{\omega}$, and phase difference $2\phi = kd_0$ for the beat note between the two laser fields at the positions of the ions. For $\Delta\omega_L = \omega_0$, the carrier Rabi rate is Ω_s . We assume the Lamb–Dicke limit, where $(\eta_{\text{str/com}} q_{\text{str/com}}^{(l/r)})^2 \bar{n}_{\text{str/com}} \ll 1$, with $\bar{n}_{\text{str/com}}$ the average occupation numbers and $\eta_{\text{str/com}} = k\sqrt{\hbar/2m\omega_{\text{str/com}}}$, the Lamb–Dicke parameters of the respective normal modes. The near-resonant terms of the red-sideband Hamiltonian are

$$\begin{aligned} \hat{H}_{\text{rsb}} = & i\hbar\Omega_s \left[\eta_{\text{com}} q_{\text{com}}^{(l)} \hat{a}_{\text{com}} \hat{\sigma}_l^+ e^{-i(\delta_{\text{com}} t - \phi_s + \phi)} \right. \\ & + \eta_{\text{str}} q_{\text{str}}^{(l)} \hat{a}_{\text{str}} \hat{\sigma}_l^+ e^{-i(\delta_{\text{str}} t - \phi_s + \phi)} \\ & + \eta_{\text{com}} q_{\text{com}}^{(r)} \hat{a}_{\text{com}} \hat{\sigma}_r^+ e^{-i(\delta_{\text{com}} t - \phi_s - \phi)} \\ & \left. + \eta_{\text{str}} q_{\text{str}}^{(r)} \hat{a}_{\text{str}} \hat{\sigma}_r^+ e^{-i(\delta_{\text{str}} t - \phi_s - \phi)} \right] + \text{h.c.} \end{aligned}$$

where $\delta_{\text{str/com}} = \Delta\omega_L - \omega_0 + \omega_{\text{str/com}}$ is the detuning relative to the red sideband of the respective normal mode, and ϕ_s is the phase of the sideband excitation at the mean position of the ions.

Spin–spin interaction. In the limit of a strongly driven carrier, such that $|\Omega_c| \gg \left\{ \eta_{\text{str/com}} \sqrt{\bar{n}_{\text{str/com}}} \Omega_s, |\delta_{\text{str/com}}| \right\}$, it is helpful to first transform to an internal-state basis where the bare spin states are dressed by the carrier^{24,25}. In this dressed frame, the basis states $\{ |+\rangle_{l/r}, |-\rangle_{l/r} \}$ are eigenstates of

$$\hat{\sigma}_{(l/r)}^{\phi_c} = \cos(\phi_c) \hat{\sigma}_{(l/r)}^x - \sin(\phi_c) \hat{\sigma}_{(l/r)}^y$$

with $|\pm\rangle_{l/r} = \frac{1}{\sqrt{2}} \left(|\uparrow_{l/r}\rangle \pm e^{-i\phi_c} |\downarrow_{l/r}\rangle \right)$ and $\hat{\sigma}_{l/r}^{\phi_c} |\pm\rangle_{l/r} = \pm |\pm\rangle_{l/r}$. For each of the four internal basis states $|\pm\rangle_l |\pm\rangle_r$ and each normal mode, the sideband interaction can be written (neglecting rapidly oscillating terms near $2\Omega_c$)

$$\begin{aligned} \hat{H}_d = & i\hbar \left(d_{\text{com}} e^{i\delta_{\text{com}} t} \hat{a}_{\text{com}}^\dagger - d_{\text{com}}^* e^{-i\delta_{\text{com}} t} \hat{a}_{\text{com}} \right) \\ & + i\hbar \left(d_{\text{str}} e^{i\delta_{\text{str}} t} \hat{a}_{\text{str}}^\dagger - d_{\text{str}}^* e^{-i\delta_{\text{str}} t} \hat{a}_{\text{str}} \right) \end{aligned}$$

where the coefficients $d_{\text{str/com}}$ are state-dependent coherent displacement rates

$$\begin{aligned} d_{\text{str/com}}(s_l, s_r) = & -\frac{\Omega_s}{2} \eta_{\text{str/com}} \left(\sin(\theta_{\text{str/com}}) s_l e^{-i(\phi_s - \phi_c - \phi)} \right. \\ & \left. + \cos(\theta_{\text{str/com}}) s_r e^{-i(\phi_s - \phi_c + \phi)} \right) \end{aligned} \quad (2)$$

with $s_{l/r} \in \{-1, 1\}$ the eigenvalues corresponding to the basis states in question. The integrated displacements $\alpha_{\text{str/com}}$ and the geometric phases $\Phi_{\text{str/com}}$ acquired after time t are³¹

$$\begin{aligned} \alpha_{\text{str/com}}(s_l, s_r, t) = & i \frac{d_{\text{str/com}}(s_l, s_r)}{\delta_{\text{str/com}}} \left(1 - e^{i\delta_{\text{str/com}} t} \right) \\ \Phi_{\text{str/com}}(s_l, s_r, t) = & \frac{|d_{\text{str/com}}(s_l, s_r)|^2}{\delta_{\text{str/com}}^2} \left(\delta_{\text{str/com}} t - \sin(\delta_{\text{str/com}} t) \right) \end{aligned} \quad (3)$$

To return the motions of both modes to the original state after an interaction duration T , we require $\alpha_{\text{str/com}}(s_l, s_r, T) = 0$. This happens irrespective of the (state-dependent) magnitude of $d_{\text{str/com}}$ if $\delta_{\text{str/com}} T = c_{\text{str/com}} (2\pi)$ with $c_{\text{str/com}}$ an integer. In such cases, the motion is displaced around $|c_{\text{str/com}}|$ full circles in the respective phase spaces of the two modes by the interaction. Also, because $\delta_{\text{str}} - \delta_{\text{com}} = 2\sqrt{\delta^2 + \Omega_{\text{ex}}^2}$, the interaction duration can assume only certain values, determined by $\Delta c \equiv c_{\text{str}} - c_{\text{com}} > 0$, for the motion to return to its original state:

$$T = \frac{\pi \Delta c}{\sqrt{\delta^2 + \Omega_{\text{ex}}^2}}$$

If the spin and motional states are in a product state initially, they will be in a product state at T and any integer multiple of T . The spin-dependent phases acquired during T simplify to

$$\begin{aligned} \Phi_{\text{str/com}}(s_l, s_r) = & \left(\frac{\eta_{\text{str/com}} \Omega_s}{2} \right)^2 \\ & \times \frac{T}{\delta_{\text{str/com}}} \left[1 + s_l s_r \cos(2\phi) \sin(2\theta_{\text{str/com}}) \right] \end{aligned}$$

The spin-dependent term is largest if $\phi = j\pi/2$ with j integer. This corresponds to the ions being spaced by an integer number of half-wavelengths π/k . In the experiment, the separation of the ions is controlled by slight changes in the well curvatures to ensure half-integer wavelength spacing. Also, $|\sin(2\theta_{\text{str/com}})|$ is reduced for $|\delta| > 0$ and eventually vanishes as the modes decouple in the limit $|\delta| \gg \Omega_{\text{ex}}$; therefore, the most efficient spin–spin interactions are implemented for $\delta = 0$. For our experimental conditions and $\delta = 0$, the mode splitting is much smaller than the average mode frequency $\bar{\omega}$, so we can approximate $\eta_{\text{str/com}} \approx \eta = k\sqrt{\hbar/2m\bar{\omega}}$. If we also assume that $\delta \ll \Omega_{\text{ex}}$, the phases simplify to

$$\begin{aligned} \Phi_{\text{str/com}}(s_l, s_r, T) = & \left(\frac{\eta \Omega_s}{2} \right)^2 \frac{T}{\delta_{\text{str/com}}} \left[1 \mp s_l s_r \cos(2\phi) \left(1 - \frac{\delta^2}{2\Omega_{\text{ex}}^2} \right) \right] \end{aligned}$$

In this limit, the phases $\Phi_{\text{str/com}}(s_l, s_r, T)$ depend only to second order on the relative detuning of the two wells. The shortest loop duration T is realized for $\Delta c = 1$, but the phase accumulates most effectively when the sideband drive is tuned to $\bar{\omega}$, exactly halfway between the normal modes ($c_{\text{str/com}} = \pm 1$, $\Delta c = 2$). At this detuning, the logical phase acquired on both modes adds constructively, and there is always some degree of phase cancellation for all other possible settings of the detuning. The total phase accumulated on both modes during T is

$$\begin{aligned}\Phi(s_1, s_r, T) &= \Phi_{\text{str}}(s_1, s_r, T) + \Phi_{\text{com}}(s_1, s_r, T) \\ &= -\cos(2\phi) \frac{(\eta\Omega_s)^2}{2\Omega_{\text{ex}}} s_1 s_r T\end{aligned}$$

For any integer multiple of T , we can summarize the action of the applied fields as

$$|\pm 1, \pm r, jT\rangle = \exp\left[-i \cos(2\phi) \frac{(\eta\Omega_s)^2}{2\Omega_{\text{ex}}} \hat{\sigma}_1^{\phi_c} \hat{\sigma}_r^{\phi_c} jT\right] |\pm 1, \pm r, 0\rangle$$

with j a positive integer. Because this holds for a complete set of spin-basis states, it also holds for any general initial state of the system. Therefore, at any multiple of T , the system evolution is equivalent to that under the spin–spin Hamiltonian

$$\hat{H}_{\text{eff}} = \hbar\kappa \hat{\sigma}_1^{\phi_c} \hat{\sigma}_r^{\phi_c} \quad (4)$$

$$\kappa = \cos(2\phi) \frac{(\eta\Omega_s)^2}{2\Omega_{\text{ex}}} \quad (5)$$

A change from ferromagnetic to anti-ferromagnetic interaction can be accomplished by a π/k change in the ion spacing, corresponding to a $\pi/2$ change in ϕ . Alternatively, for example, $\kappa' = -\kappa/3 < 0$ is realized with a choice of detuning such that ($c_{\text{str}} = -1$, $c_{\text{com}} = -3$).

In principle, we can either perform a ‘stroboscopic’ emulation with the total duration a multiple of T , or use detunings $\delta_{\text{str/com}}$ whose magnitudes are much larger, so that all $|\alpha_{\pm}| \ll 1$ for any given time. For all multiples of T , the motional states of the ions factor from the spin states, so if one only ‘looks’ stroboscopically at times jT , the system effectively appears as though only the spins have evolved according to equations (4) and (5), while the motion has returned to its original state, thus appearing to have been unaffected. For much larger magnitude detunings $\delta_{\text{str/com}}$ spin–motion entanglement, and, thus, the deviation of the simulated state from that under the ideal spin–spin interaction, is small for arbitrary durations of the interaction²⁶. The added robustness comes at the expense of a weaker spin–spin interaction, which has to be compensated for by higher drive power or longer simulation timescales. Finally, rather than suppressing the bosonic harmonic oscillator modes, we can include them as an integral part of the simulator and study collective spin–boson Hamiltonians, which have been recently shown to contain complex behaviour comparable to models with only spin–spin interactions³².

Experimental characterization. We benchmark the spin–spin Hamiltonian of equations (4) and (5) by using it to entangle the hyperfine states (pseudo-spins) of two ions starting from the initial state $|\downarrow\downarrow\rangle$. To gain isolation from small errors, we break the total spin–spin interaction into two loops in phase space with $\kappa = \pi/8$ for each loop. For the first loop, we can choose $\phi_c = 0$ and $\phi_s = 0$ so that the eigenstates in the dressed basis are those of $\hat{\sigma}_{1/r}^x$. After finishing the first loop, we change carrier and sideband phases to $\phi_c = \phi_s = \pi$. The change in carrier phase is such that at the end of the second loop, the rotating frame due to the carrier is re-aligned with the frame of the bare states. This is because rotations around the x axis of the Bloch sphere in the first loop are unwound by rotating around the $-x$ axis for the same duration in the second loop. In addition, the phase change in the sideband drive ensures that $d_{\text{str/com}}(s_1, s_r)$ of the first loop is followed by $-d_{\text{str/com}}(s_1, s_r)$ in the second loop. In total there are three sign changes in the displacement rate equation (2), the first from replacing $\hat{\sigma}_{1/r}^x$ by $\hat{\sigma}_{1/r}^{-x} = -\hat{\sigma}_{1/r}^x$ and therefore $s_{1,r} \rightarrow -s_{1,r}$, the second due to $\phi_c = 0 \rightarrow \pi$ and the third due to $\phi_s = 0 \rightarrow \pi$, which multiply to change the sign of the displacement rate. As a consequence, the total displacement $\alpha_{\text{str/com}}(s_1, s_r, T)$ in the second loop (equation (3)) is equal and opposite to that in the first loop and the motional wavefunctions return to their original positions in phase space even if $\alpha_{\text{str/com}}(s_1, s_r, T) \neq 0$ due to small errors in the detunings $\delta_{\text{str/com}}$ or in loop duration, provided that those errors are constant over both loops³³. The phases $\Phi_{\text{str/com}}(s_1, s_r)$ depend only on $|d_{\text{str/com}}(s_1, s_r)|^2$, and the effective spin–spin evolution is therefore the same in both loops. With the sideband excitation tuned to $\bar{\omega}$, a single loop duration corresponds to $T_L = 2\pi/\Omega_{\text{ex}}$ for a total interaction duration of $2T_L$. Starting from the initial state $|\downarrow\downarrow\rangle$, we would ideally produce the maximally entangled state $|\Psi_e\rangle = \exp\left[-i \frac{\pi}{4} \hat{\sigma}_1^x \hat{\sigma}_r^x\right] |\Psi_i\rangle = \frac{1}{\sqrt{2}}(|\downarrow\downarrow\rangle - |\uparrow\uparrow\rangle)$, if the sideband Rabi frequency satisfies $\eta\Omega_s = \Omega_{\text{ex}}/2\sqrt{2}$.

Determination of probabilities from state-dependent fluorescence. During one detection period (300–400 μs) we typically detect between 0.15 and 0.6 counts if both ions are projected into $|\uparrow\rangle$, and 3 to 5 additional counts for each ion in state $|\downarrow\rangle$. For each experimental setting, we record count histograms for 200–500 experiments.

Consider a count histogram $h = (h(i))_i$, where $h(i)$ experiments yielded i counts and $N = \sum_i h(i)$ is the total number of recorded counts. We infer the probabilities P_b with $b = 0, 1, 2$ by applying probability estimators $w_b = (w_b(i))_i$ to h according to $P_b = \sum_i w_b(i)h(i)/N$. The probability estimators are determined from the recorded

photon counts for on-resonance microwave Ramsey experiments with two ions, where the phase ϕ of the second $\pi/2$ -pulse was varied. These experiments are performed before and after the experiments to be analysed. An ideal such Ramsey experiment satisfies

$$P_0(\phi) = \cos^4(\phi/2)$$

$$P_1(\phi) = \sin^2(\phi/2)$$

$$P_2(\phi) = \sin^4(\phi/2)$$

The histograms h_ϕ recorded at phase ϕ are sampled from the mixture $P_0q_0 + P_1q_1 + P_2q_2$, where the q_b are the count distributions for zero, one or two bright ions. From this model and the Ramsey data, we can determine w_b so that $\sum_i w_b(i)h_\phi(i)$ yields $P_b(\phi)$. We use a linear least-squares fit, regularizing it to minimize the anticipated variance when inferring P_b for the completely mixed state.

Given a probability estimator w and a recorded histogram h , we estimate the experimental variance of the inferred probability P according to $v = (\sum_i w(i)^2 h(i)/N - P^2)/(N - 1)$. This variance determines the error bars in Fig. 3. For the fidelities and related quantities, the variation in the probability estimators due to the finite statistics of the Ramsey experiments contributes an error comparable to this variance. To determine the overall statistical error in the fidelities, we used non-parametric bootstrap resampling³⁴ on all contributing histograms with 100 bootstrap resamples to determine error bars for fidelities and contrasts.

The assumed model for the Ramsey experiments makes no assumptions about the shapes or relationships of the count distributions q_b . This was important because we found that the q_b exhibit clear deviations from Poissonian distributions. We also determined c_b , the mean number of counts according to q_b , and found that $c_2 - c_0$ exceeded $2(c_1 - c_0)$ by about 8% for all the Ramsey scans considered.

Several effects result in deviations from an ideal Ramsey experiment. We found that there is a phase offset of approximately 5° in the Ramsey scans. We shifted the phase accordingly before determining the probability estimators. This had a statistically negligible effect on inferred probabilities and fidelities. After adjusting for the phase shift, we found no signature of a mismatch between the model and the data. In addition to checking that the dependence of the histograms on the phase was as expected, we considered whether there are more than three count distributions contributing to the Ramsey scans. We found no signature of such an effect. Furthermore, all other histograms, including those used to determine fidelities, could be explained as arising from a mixture of the same three count distributions.

An important effect that need not be apparent from the data is state-preparation error. By simulating Ramsey experiments with state-preparation error and q_b as inferred from the data, we determined that such errors lead to systematic overestimates of fidelities that are well correlated with the state-preparation error. The simulations involved initial states that are mixtures of the basis states. Let ϵ ($\ll 1$) be the probability that the state in this mixture is not $|\downarrow\downarrow\rangle$. For the inferred fidelities, we estimate a systematic increase in fidelity of approximately 1.1ϵ . The quoted systematic errors are based on a pessimistic upper bound of 0.01 on ϵ . In inferring P_b for a single histogram (as required for the plots in Fig. 3), these biases are small compared with the statistical error and were therefore not included in the error bars. We assumed that pulse errors had a statistically small effect on inferred probabilities and fidelities.

Discussion on robustness of analogue simulations. Richard Feynman stated that, ‘with a suitable class of quantum machines you could imitate any quantum system, including the physical world’³¹. For arbitrarily precise quantum simulations, this requires scalable quantum computers that employ error correction, but realizing these computers has proven to be very difficult. An alternative that may circumvent the difficulties is to faithfully map the dynamics of the physical model of interest onto sufficiently controllable quantum systems. This is called ‘analogue quantum simulation’. Because the overall physical properties of interest are often determined by local observables, the expectation is that the full quantum state need not be arbitrarily precise for useful information to be obtained³⁵. For example, although the global many-body state of the simulator is sensitive to a local perturbation, the expectation values of intensive properties can be more robust³⁰. It is also noteworthy that many material properties are robust in the presence of naturally occurring imperfections. This suggests that a useful analogue quantum simulator might be significantly easier to construct than a quantum computer, even in the absence of sufficiently precise quantum gates or explicit quantum error-correction strategies needed for fault tolerance³⁶.

Although the robustness of analogue quantum simulations is frequently asserted, it is not a simple matter to quantify the effects of experimental imperfections on physical properties of interest. At present, there does not exist a perfect and rigorous way to assess the quality of the results that one can expect from an analogue quantum simulation³⁰. Nevertheless, one can seek models and conditions for which the effects of the quantum simulator’s imperfections are expected to be minor and well

understood. A number of experimental groups, across multiple platforms, are currently pursuing this strategy. An alternative is to seek validation of the results on small systems that can be classically verified before obtaining results on large systems realizing the same model. In addition, validation may come from consistent results on multiple independent simulator platforms. This can eliminate simulator artefacts, as has been suggested in ref. 37.

For many developers of quantum simulators, a common Hamiltonian for testing their setups is the transverse Ising model^{4,8,10,22,23,26}. Recently, a theoretical investigation into the influence of disorder on the fidelity of quantum simulations of the Ising model was performed³⁰. With relatively large spin chains, analogue quantum simulator results are predicted to be usefully robust to random variation in the coupling coefficient up to a few per cent. This high tolerance to coupling imperfections, relative to a comparable universal quantum computation, is achieved because the simulation required that only local observables, rather than the entire simulator state, be robust. Although this work does not account for other technical issues that often limit the performance of experiments, it is nonetheless a useful performance indicator. In relation to our work, it suggests that although further progress on reducing experimental imperfections is probably required, the future technical improvements we propose may be sufficient. It may also be possible to ensure that the experimental imperfections correspond to physically relevant effects in the model under consideration. For example, Lloyd suggested that, “decoherence and thermal effects in the quantum computer can be exploited to mimic decoherence and

thermal effects in the system to be simulated”², as was recently demonstrated³⁸. To ensure that the platform’s imperfections represent physically relevant interactions between the model and its normal environment, one can sometimes engineer the mapping from the ideal model to the experimental platform³⁹. Although we cannot make a general statement on the robustness of analogue quantum simulations, the above discussion is suggestive and many promising examples have been proposed.

31. Leibfried, D. *et al.* Experimental demonstration of a robust, high-fidelity geometric two ion-qubit phase gate. *Nature* **422**, 412–415 (2003).
32. Jünemann, J., Cadarso, A., Pérez-García, D., Bermudez, A. & García-Ripoll, J. J. Lieb-Robinson bounds for spin-boson lattice models and trapped ions. *Phys. Rev. Lett.* **111**, 230404 (2013).
33. Hayes, D. *et al.* Coherent error suppression in multiqubit entangling gates. *Phys. Rev. Lett.* **109**, 020503 (2012).
34. Efron, B. & Tibshirani, R. J. *An Introduction to the Bootstrap* (Chapman & Hall, 1993).
35. Cirac, J. I. & Zoller, P. Goals and opportunities in quantum simulation. *Nature Phys.* **8**, 264–266 (2012).
36. Knill, E. Quantum computing. *Nature* **463**, 441–443 (2010).
37. Leibfried, D. Could a boom in technologies trap Feynman’s simulator? *Nature* **463**, 608 (2010).
38. Li, J. *et al.* Motional averaging in a superconducting qubit. *Nature Commun.* **4**, 1420 (2013).
39. Tseng, C. H. *et al.* Quantum simulation with natural decoherence. *Phys. Rev. A* **62**, 032309 (2000).